Materials Science and Engineering B 299 (2024) 116985

Contents lists available at ScienceDirect

Materials Science & Engineering B

journal homepage: www.elsevier.com/locate/mseb

Structural, dielectric, thermoelectric, and magmatic properties of Er^{3+} ion substituted Mg-Zn spinal nanoferrites: High charge-storage capacitors and high-frequency microwave device applications

Banoth Baburao [a], N. Hari Kumar [b,*], Avula Edukondalu [a,c], D. Ravinder [a,*]

[a] Department of Physics, University College of Science, Osmania University, Hyderabad 500020, India
[b] Department of Physics, St.Mary 's Group of Institutions, Deshmukhi, Yadadri Bhongiri 508116, India
[c] Department of Physics, University Post Graduate College, Secunderabad, Osmania University 500003, India

ARTICLE INFO

Keywords:
Structural studies
Optical studies
Dielectric properties
Thermoelectric power studies
Low temperature 300K-100K properties

ABSTRACT

The Er-substituted magnesium and zink ferrite nanomaterials with the chemistry formula $Mg_{0.8}Zn_{0.2}Er_xFe_{2-x}O_4$ (x = 0.00, 0.005, 0.01, 0.015, 0.02, 0.025) were generated in the study utilizing the citrate-gel auto combustion method. XRD is being used to investigate the cubic spinal structural structure. A transmission electron microscope (TEM) and a field emission scanning electron microscope (FESEM) were used to examine surface morphology. From the structural studies, the crystal sizes range from 14.46 to 96.40, with lattice parameters ranging from 8.434 to 8.449 and X-ray density (gm/cc) ranging from 4.585 to 4.671 and porosity (%) ranging from 7.67 to 7.91. The resulting macrostrain produces internal tension and can impair material grain growth. UV–visible absorption spectroscopy gives grain size pictures as well as quantifications at 300 K and 100 K, respectively. The wavelength range cut-off from 537.6 nm to 270.9 nm. The dielectric characteristics of the samples were tested at room temperature using an LCR meter at various frequencies. The dielectric parameters include the real component of the dielectric constant, the dielectric constant's imaginary portion, and the loss tangent. For each sample, the loss tangent of nanoferrites fell as the frequency increased. This type of material is used in capacitors and microwave devices. Thermoelectric power studies measured all samples. From the studies observed, the seeback coefficient decreases with increasing temperature and Er doping. The room temperature and low temperature magnetic properties were studied at 300 k and 100 k at low temperature ZFC and FC. The blocking temperature T_b was around 300 K.

1. Introduction

Spinel ferrite is a ferrite material that has a cubic spinel structure and the chemical formula AB_2O_4, where A' is the divalent cation and B' denotes the trivalent metal ion [1–2]. Ferrites, both in bulk and nanoform, are used in a variety of commercial and scientific applications. These substances are useful in a variety of applications, including storage devices, tapes with magnets, magnetic hypothermia, MRI, a transformer and the inductor core gadgets, electrical protection, multiple-layer chip inductors that are antenna devices, microwave absorbers, sensors for temperature, magnetic cooling, and others [3]. Many scientists worked on the production and characterization of the aforementioned materials when doped with various components [4–6].

In the setting of Mg-Zn iron oxide inverse spinel structure, mg^{2+} cations usually choose octahedral (B) positions [7–8]. The Fe^{3+} ions on the other hand exhibit a high preference for the tetrahedral (A) sites. In contrast, magnesium ferrites (MF) and MFs-based materials were specifically confined to potential microwave device applications such as circulation systems, antennas, electrodes, and so on. Because of their strong saturation magnetization (Ms), low Curie temperature (Tc), and other magnetic fields with minimal loss [9]. It also depends on synthesis and stereometric chemical composition.

Ferrites can be produced using a variety of methods, including hydrothermal microwaves [10], explosive combustion [11], co-precipitation [12], and solution gel techniques [13]. When all of these synthesis processes were compared, the citrate gel autocombustion method was found to be the most appealing owing to its utilization of low operating temperatures, short reaction durations, homogenous

* Corresponding authors.
E-mail addresses: aknhkou@gmail.com (N. Hari Kumar), ravindergupta28@rediffmail.com (D. Ravinder).

https://doi.org/10.1016/j.mseb.2023.116985
Received 22 May 2023; Received in revised form 29 August 2023; Accepted 25 October 2023
Available online 31 October 2023

material combinations, tiny (nano)-sized particles, and so on [14–15]. Because rare earth ions have higher ionic radii than Fe^{3+}, they substitute Fe^{3+} in ferrite and reduce the spinel lattice's solubility [16–18]. Rare-earth ions have been shown to be effective additions for improving the magnetic characteristics of ferrite.

In this paper, we offer a straightforward approach for synthesizing nanoparticles of Mg-Zn ferrite utilizing metal nitrates and citric acid extract solution as precursors. XRD, FE-SEM, TEM, and dielectric and magnetic characteristics were used to describe the samples. The current work aims to evaluate how Er^{3+} ion doping impacts the electrical and magnetic properties of Mg spinel ferrites, as well as whether they are suitable for switching and memory storage devices.

2. Experimental procedure

$Mg_{0.8}Zn_{0.2}Er_xFe_{2-x}O_4$ (x = 0.00, 0.005, 0.01, 0.015, 0.02, 0.025) are prepared using the citrate gel auto-combustion method. Precursors include citric acid, magnesium nitrate, zinc nitrate, erbium nitrate and ferric nitrate. The materials utilized were of analytical quality and did not require additional purification. In all trials, distilled water was utilized. The Zn, Mg, and Er chemicals were weighed using a stoichiometric ratio. The measured amounts of metal nitrates were then dissolved in a tiny quantity of distilled water and agitated for 1 h to get a clear, uniform solution. The metal nitrate/citric acid ratio was kept constant at 1:3 for all samples, yielding the nitrate-citate resolution. The ammonia solution was then added to the solution drop by drop in order to maintain a pH of 7. We created an ammonia solution and added it in varying concentrations to the nitrate-citrate combination until it reached a pH of around 7. The solution was combined and heated for 10–12 h with constant stirring at 100 °C. As a result of this, a viscous gel formed. The water in the combination evaporated, resulting in a dry gel that creates internal combustion and produces a brown-colored product. The acquired powder sample was manually ground using agate mortars before being calcined at 500 °C for 4 h in a typical furnace. Based on the requirements, various characterization methods, such as an X-ray diffractometer, were used on these powder samples. Transmission electron microscope, field-emission scanning electron microscope, UV–visible absorption spectroscopic microscope, dielectric and magnetic properties. The dielectric properties were studied at 20 Hz^{-1} kHz on an LCR (AUTOLAB) (PGSTAT30) meter at room temperature. Magnetic properties were analyzed by VSM (vibratory sample magnetometer) with the 10-mark II VSM model at variation temperature.

3. Results and discussions

3.1. XRD analysis

Fig. 1 XRD patterns shows the X-ray density, lattice constant, and molecular weight of $Mg_{0.8}Zn_{0.2}Er_xFe_{2-x}O_4$ (x = 0.00, 0.005, 0.01, 0.015, 0.02, 0.025) nanoparticles. The diffraction pattern clearly shows that cubic spinel structures formed in all samples [19]. It is possible that this occurred as a result of their exposure to conventional heating in part [20]. The lattice constant was computed using the exact least squares method for all samples. The obtained lattice constant drops as the erbium concentration of the ferrite compounds increases. the crystal sizes range from 14.46 to 96.40. The values of X-ray density for all compositions were also determined. The general trend of X-ray density with Er-addition for all compositions indicates an increase, demonstrating Er ion solubility in the spinel structure [21]. A conventional formula was used to calculate the constants of the lattice (a = b = c) for the strongest (3 1 1) peak of all samples [22]. where is the interplanar distance for the (3 1 1) reproduction plane and the Miller indices h, k, and l [23–25].

It is generally understood that erbium ions preferentially occupy the tetra (A) and octa (B) sites [26]. According to the literature, the predominant concentration of erbium ions occupies the B-site, while the

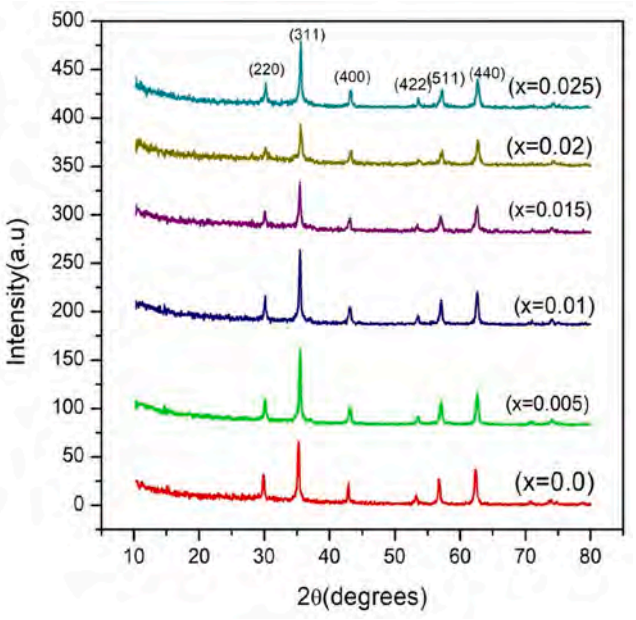

Fig. 1. XRD patterns of Er substituted Mg-Zn nano ferrites.

minority content may be found at the A-site. As a result, this type of environment promotes unit cell growth as well as lattice macrostrain [27]. The produced macrostrain, in turn, causes internal stress and can impede material grain development. It is clear that the theoretical densities of × = 0.0 to 0.01 samples were raised and found to be greater than the underlying materials' theoretical densities [10]. Erbium ions are replaced in the × = 0.0 to × = 0.01 ferrite system, and the molecular weight of the materials increases [28].

3.2. Surface morphology

TEM and FESEM were used to investigate the surface morphology of the all nanoparticles [31]. Figs. 2 and 3 show FESEM and all samples' TEM with SAD images at the chosen 100 nm region of the spot. The topographic properties of the generated samples were examined using FESEM and TEM [32]. TEM and SAD pictures revealed that the bulk of the nanoparticles had a spherical form and were thin, with only a few elongated particles. The FESEM images of nanoparticles showed clusters resembling grains, which were clearly seen in the figures. The heavily interacting grains were detected in the × = 0.005 (Fig. 2) specimen [33]. This behavior might be explained by the significant magnetic contact between the grains. Nonetheless, a few spherical stones that resemble grains, as well as a few agglomerated grains, were created in the × = 0.01 (Fig. 2) material. Apart from that, the grain size of the current materials was determined using the rectilinear interrupt approach. The results were found to differ across all materials. This proved that there is a significant disparity between particle and grain sizes. Overall, it is proven that the produced nanoparticles contain no contaminant components [34].

Er-doped magnesium-zink ferrite displayed nanoparticle-like spheres. The nicely agglomerated nanoparticles were generated when the magnesium ferrite system was supplemented with Er-element [33]. In other words, one might think of it as nanoparticles heaping up on top of each other. The latter's average particle size was discovered to be in the range of 19–45 nm. This proved that there was a significant difference between grain and particle size [35]. This is smaller than the particle size of nanoferrites generated chemically [36–39]. The elemental percentages of Mg, Zn, Er, and Fe are studied and shown in Fig. 4. The atomic wait of the samples was normalised and conformed.

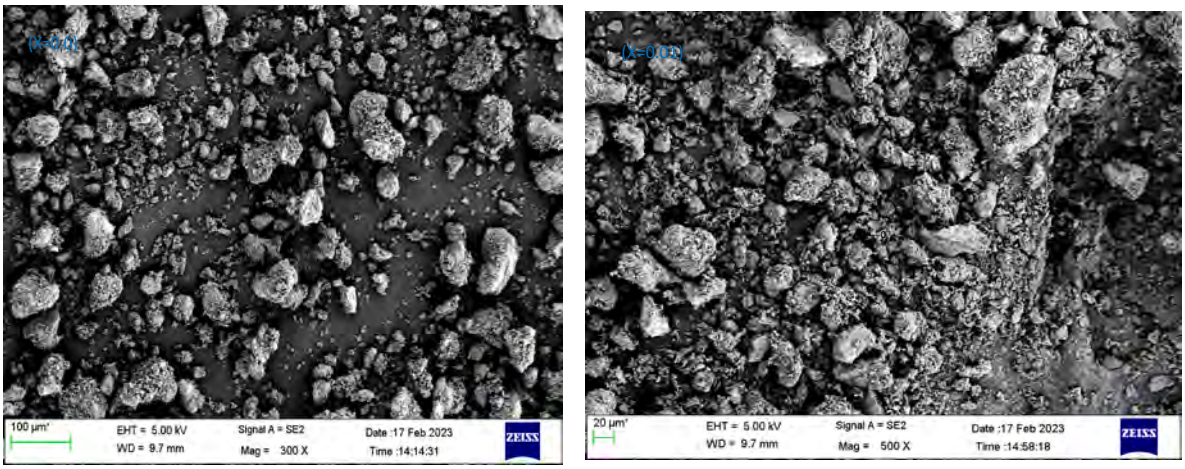

Fig. 2. SEM images of Er substituted Mg-Zn (x = 0.0 and 0.01) nano ferrites system.

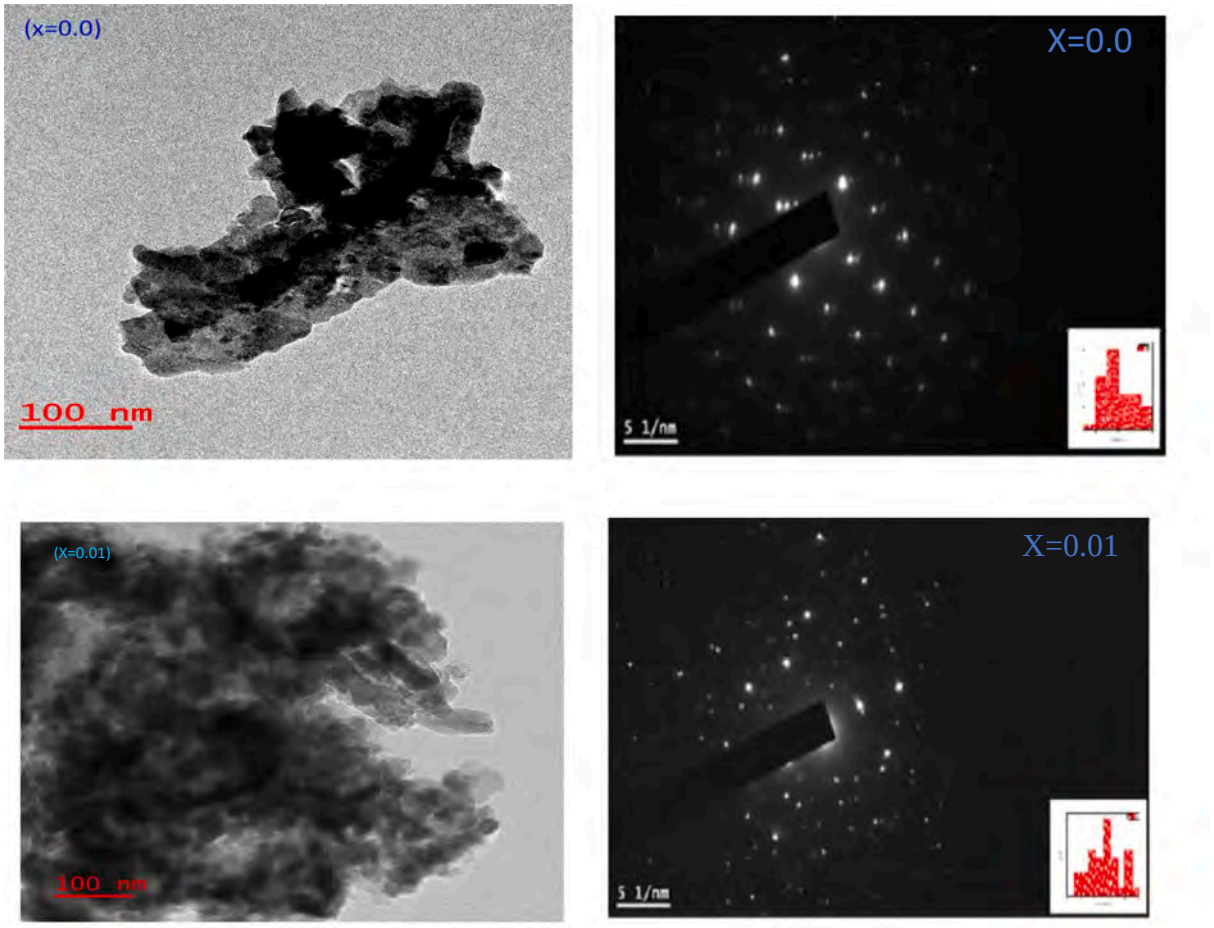

Fig. 3. TEM/SAD images of Er substituted Mg-Zn (x = 0.0 and 0.01) nanoferrites.

3.3. *Uv–visible absorption spectroscopy*

The measurement of optical absorption spectra is among the best ways for assessing and developing energy gaps and band structures in materials that are crystalline and non-crystalline [40]. The gap energy (Eg) represents the optical band gap altitude indicated in Table 1. In other words, it represents the amount of energy compulsory by a charge carrier to transition from to the conduction band from the valence band. The Tauc relation [29] can be used to calculate this energy:

$$\alpha h\upsilon = A(h\upsilon - Eg)n$$

where α is the coefficient of absorption, hυ is the incident wave's energy, and n is relevant to the type of the transition. It is equivalent to 1/2 or 2 for a straight or indirect transition, respectively [30].

The greatest wave length of Er-substituted Mg-Zn ferrites are 537.6 nm, and it is in the observable region [41]. It depicts absorbance vs

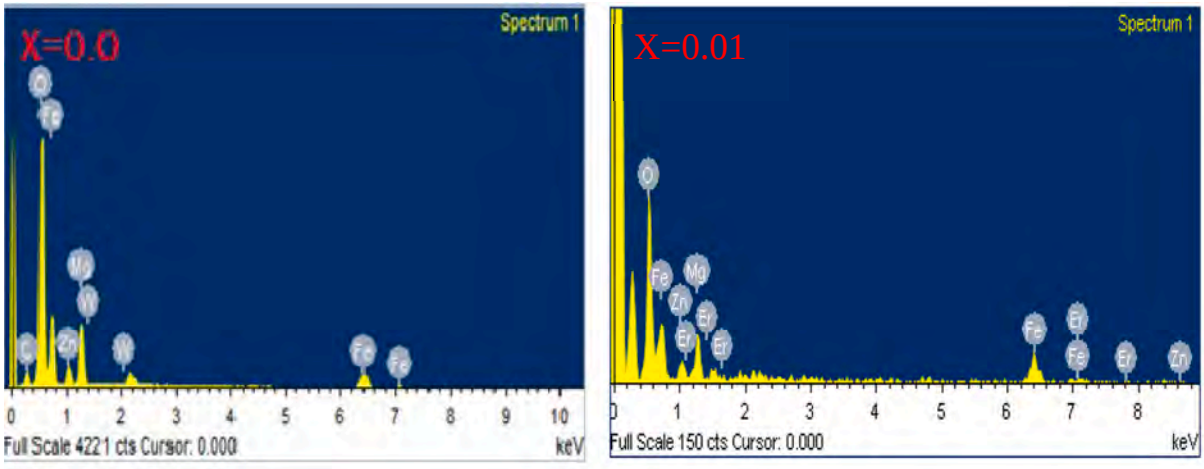

Fig. 4. EDAX images of Er substituted Mg-Zn (x = 0.0 and 0.01) nanoferrites.

Table 1
Bandgap energies of Er substituted Mg-Zn nanoferrites.

$Mg_{0.8}Zn_{0.2}Er_xFe_{2-x}O_4$	Bandgap energy(eV)
X=0.0	537.6
X=0.005	534.8
X=0.01	470.6
X=0.015	372.8
X=0.02	305.7
X=0.025	270.9

wavelength in a visual representation in Fig. 5. When Er concentration increases, the wavelength decreases, and the absorbing rim shifts from 270.9 nm to 537.6 nm. For composition × = 0.005 in Mg-Zn, there occurs a blue shift. ferrite with Er substituted; this might be caused by a low band gap due to greater particle size [42].

The O-3p orbital functions as well as the valence band, as well as the d orbital acts as the band of conduction in determining the band configuration of an Er-Zn ferrite. The Er-Zn ferrite's visible light absorption spectrum is considered to be caused by excitation of electrons from the O-3p to the Fe-4d levels, with a wavelength range cut-off from 537.6 nm to 270.9 nm, as seen in Table 1 [37]. It has been discovered that the composition influences the location of the absorption bands. Because of their large band gaps, the present compounds might be helpful in detectors, photography, and optical electronics [43].

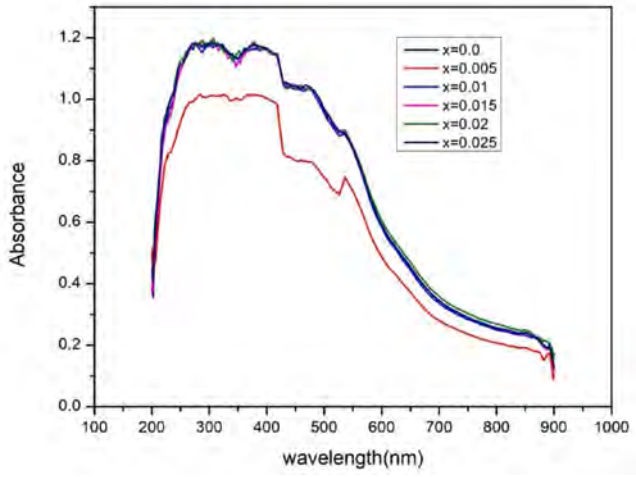

Fig. 5. UV–visible absorption spectroscopy of Er substituted Mg-Zn nanoferrites.

3.4. *Dielectric properties*

Figs. 6, 7 and 8 illustrate the frequency variation of the dielectric constant real (έ), imaginary(ë) and dielectric loss (tan δ) of Er-doped Mg-Zn samples at room temperature [38]. The versus frequency figure revealed that tan δ began to decrease as frequency increased from 200 Hz to 10 MHz. It was typical of ceramic materials' dielectric behaviour for all samples to decrease with increasing frequency. The Koop's phenomenon, often known as the dielectric model with two layers, gave a theoretic explanation for reaching higher levels and tan δ at lower frequencies [36]. Grain boundaries and grains, where grains can have a high conductivity, whereas grain limits can have poor conductivity [44]. As a result, additional charge carriers collected where the grain border meets, resulting in high έ, ë, and tan δ.

With collective frequency, the numerical values of έ, έ and tan δ decreased. Both the dielectric constant and the έ, ë and tan δ were raised. It is due to the rise in polarization with increasing temperatures [35]. At 200 Hz, the dielectric constant indicated high standards for all materials, ranging from 400 to 450 in magnitude [40]. At 4 MHz, identical parameter values of order 1–25 were observed. This confirmed the fact that all of the materials had a large dielectric constant at low frequencies, whereas at high frequencies, it was low. This might be due to the polarization decaying at the appropriate applied field frequencies, from high to low.

. The consistent trend of έ, ë and tan δ at higher frequencies was primarily chosen because of the constant polarization of the space

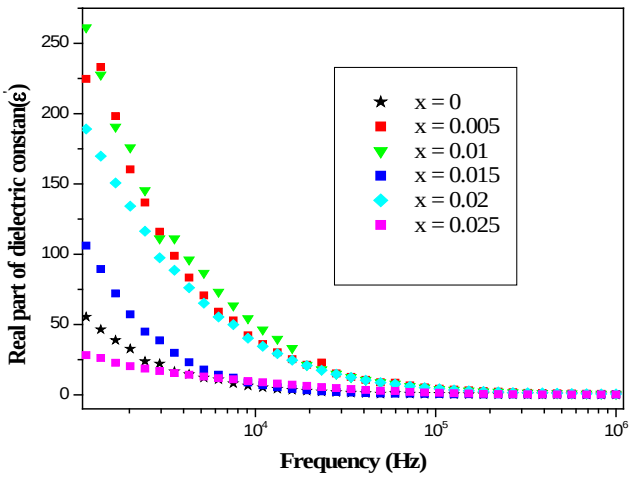

Fig. 6. Dielectric constant real part of Er substituted Mg-Zn nanoferrites.

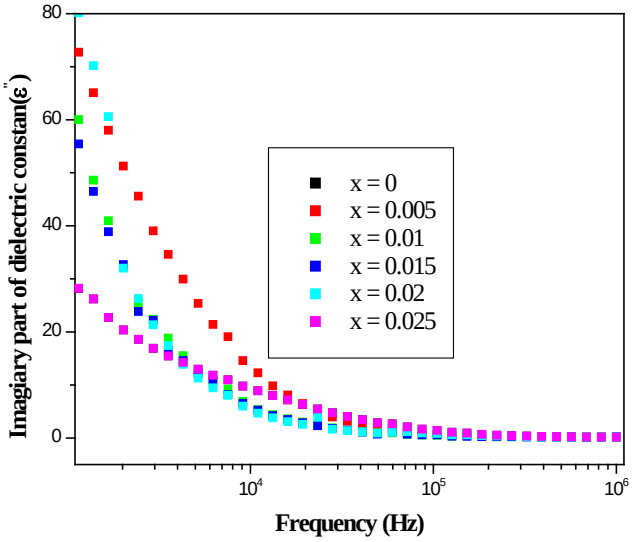

Fig. 7. Dielectric constant imaginary part of Er substituted Mg-Zn nanoferrites.

charge [39]. Similarly, the values of dielectric loss were found to be 1500–3500 at the 150 Hz frequency shown in Fig. 8. Nevertheless, at higher frequencies, these values were not seen and were estimated to be in the range 49–95 [30]. These high-lossy materials have prospective uses as dielectric absorbers, whereas materials with high dielectric constant have potential uses such as charge-stored capacitors and high-frequency microwave devices [45]. Because of the doping of Er in Mg-Zn, the inhibition of surface external conduction may reduce dielectric losses in the entire spectrum, suggesting very low signal loss while travelling through these materials. The dielectric loss angle is also affected by stoichiometry (Fe^{2+}) data, and structural or operational homogeneity is determined by the compost design and sample sintering temperatures.

3.5. Thermoelectric properties

The thermoelectric power of prepared samples was studied using a differential approach from room temperature. Fig. 9 depicts the temperature dependence of the Seebeck coefficient ($S = \frac{V}{T}$) of produced Er nanoferrites. All of the samples exhibited comparable thermal fluctuations with the Seebeck coefficient. The S' dropped as the temperature increased up to a point known as the transition temperature (Tc). However, the S' value was further lowered above the Tc. Table 2 shows the values of the samples that revealed the P-type semiconducting nature of the produced all ferrite samples without pure samples. The Seebeck coefficient was observed to decrease with increasing temperature and Er concentration [25]. The Seebeck coefficient falls and subsequently increases with temperature fluctuation. Then, although the sample behavior was revealed to be P-type semiconductor activity, the pure behavior shifted to N-type to P-type transition behavior [32].

4. Low temperature magnetic properties

The cold ZFC curves in Fig. 10 were traced by rising the temperature from 100 to 300 K and then lowering it from 300 to 100 K. It is evident that the material's ZFC and FC curves split below 290 K, and so this temperature is referred to as the blocking temperature. As a result, at temperatures higher than the freezing point, the moment of magnetism of a continuous unblocking of a single-domain nanoparticle is possible [46].

From Fig. 11, the M−H curve is nearing thermal equilibrium by functioning as though it were an atomic paramagnet. That was demonstrated in the M−H loops logged in the first quadrant. The whole

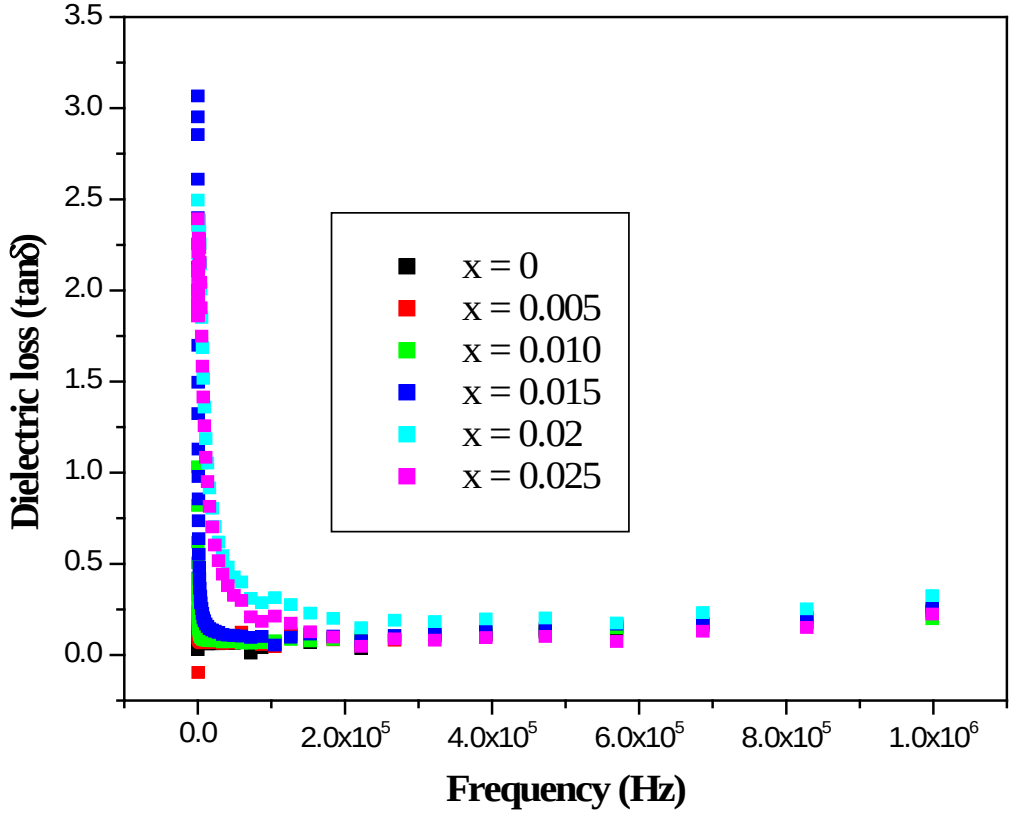

Fig. 8. Dielectric loss (tanδ) of Er substituted Mg-Zn nanoferrites.

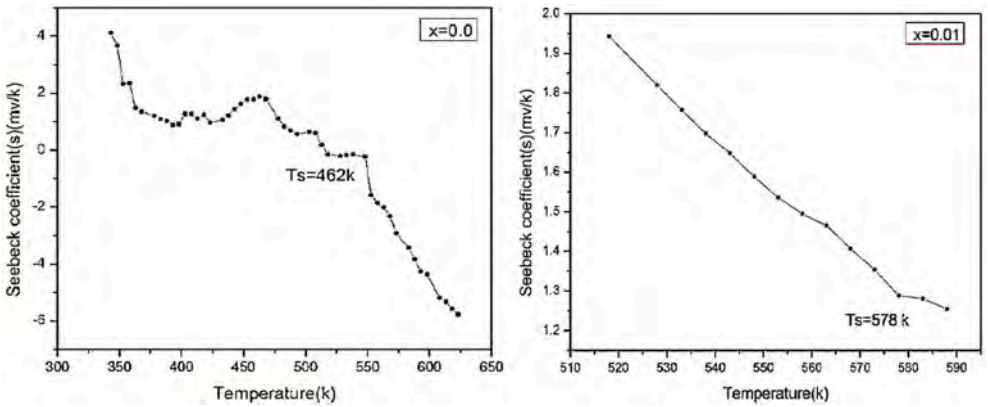

Fig. 9. Dielectric constant real part of Er substituted Mg-Zn nanoferrites.

Table 2
Bandgap energies of Er substituted Mg-Zn nanoferrites.

$Mg_{0.8}Zn_{0.2}Er_xFe_{2-x}O_4$	Ts(K)	Tc(K)	S(mV/K)
0.0	423	423	423
0.005	498	498	498
0.01	378	378	378
0.015	398	398	398
0.02	413	413	413
0.025	383	383	383

M−H loop was sketched for × = 0.0 over the 100 K and 300 K magnetic field ranges. As a result, these properties are ideally suitable for converters, inductance cores, record skulls, microwave equipment, and magnetic barriers, as mentioned in previous reports [42].

The paramagnetic character was demonstrated by both the ZFC and FC curves. To calibrate the magnetization behaviour, it changes with temperature variations. The highest value for × = 0.0 material was determined to be 100 K. The superparamagnetic properties of the × = 0.005 sample were demonstrated at 300 K. At 100 K, the weak, soft nature of ferrite was seen. This indicated that the magnetic moment of × = 0.01 increased when Er was replaced in the magnesium ferrite system [43].

The particles show superparamagnetic behavior at a particular temperature. At some temperatures, cooling superparamagnetic particles causes the measurement time to be inadequate for complete magnetic relaxation. T_b is the blocking temperature. Magnetic nanoparticles display hysteresis below T_b due to metastability, not domain wall motion. Thermal excitations cause the magnetic moments of distinct particles to be randomly oriented at the blocking temperature [44]. This is in contrast to the Curie temperature T_C, where heat energy randomized the spins of individual particles; in general, $T_b \ll T_C$. Magnetic torque causes to rotate a magnetic particle in a homogeneous magnetic field. Brownian rotation differs from Neel rotation in that the particle remains fixed in space but its magnetization orientation rotates. A spatially variable magnetic field is required to propel the particle [45].

5. Conclusion

The citrate-gel auto combustion method was utilized to create Er substitution Mg-Zn nanoferrites with × = 0.00, 0.005, 0.01, 0.015, 0.02, and 0.025 nanoferrites. The XRD patterns demonstrate the creation of the cubic spinel structure. With increasing Er content, the values of the constant of lattice and crystallite size fell. The hopping of charge carriers caused the conduction process in ferrites to be noticed. The particles had virtually spherical in form, and the TEM revealed the average particle size. FESEM was used to analyze the morphology. Spectroscopy of UV–visible absorption and materials with a high loss rate may have potential uses in the form of dielectric absorbers, whereas high-dielectric constant materials may have high-frequency applications, including charge-stored capacitance and microwave ovens. The seebeck coefficient linearly decreases with temperate. The TEP studies

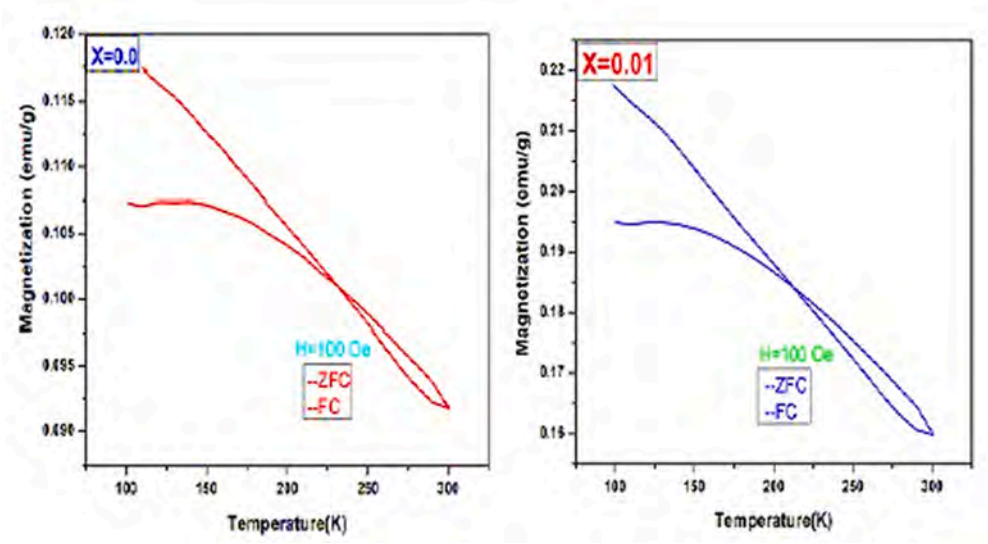

Fig. 10. ZFC & FC curves of Er substituted Mg-Zn (x = 0.0 and 0.01) nanoferrites.

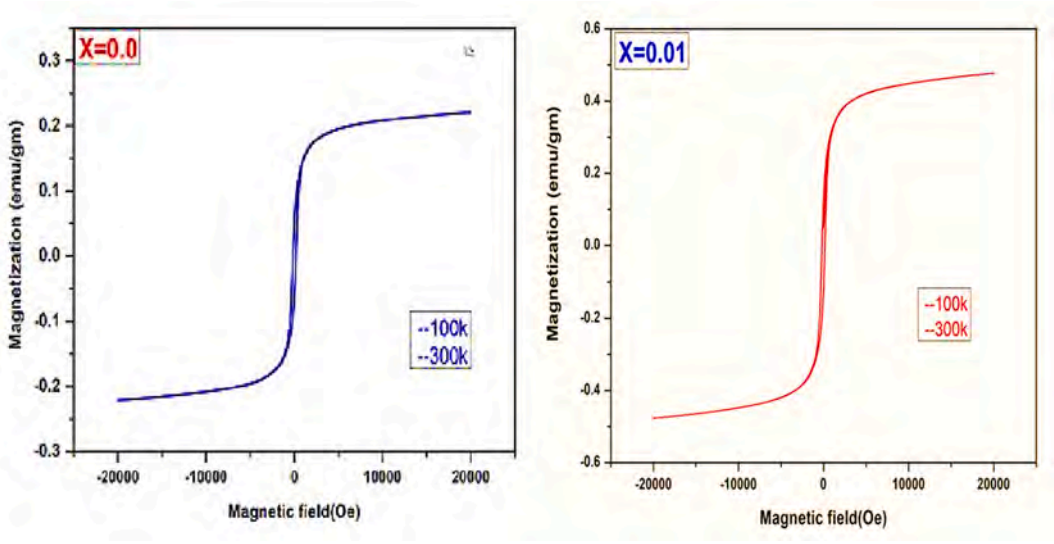

Fig. 11. M–H curves of Er substituted Mg-Zn (x = 0.0 and 0.01) nanoferrites.

for all samples shown P-type semiconductor nature except pure sample. The magnetic properties studied at low and room temperatures. The samples were exabits soft and super magnetic behaviour.

Declaration of Competing Interest

The authors declare that they have no known competing financial interests or personal relationships that could have appeared to influence the work reported in this paper.

Data availability

The data that has been used is confidential.

Acknowledgment

Thanks to SV-TPTY, Head and BOS Department of physics, university college of science, Osmania university, Hyderabad.

References

[1] LIU,Jin-xue. LIU, Ke. DU, Wen-bo. LI, Shu-bo. WANG, Zhao-hui. DU, Xian. SUN, Cui-cui. Effect of temperature on microstructure and texture evolution of Mg-Zn-Er alloy during hot compression. Trans.Nonferrous Met.Soc.28(2018)2214-2225. https://doi.org/10.1016/S1003-6326(18)64866-6.

[2] Dong-song, YIN. Er-lin, ZHANG. Song-yan, zeng. Effect of Zn on mechanical property and corrosion property of extruded Mg-Zn-Mn alloy. Trans. Nonferrous Met.Soc.18(2008)763-768. https://doi.org/10.1016/S1003-6326(08)60131-4.

[3] Zhang , Jing. Dou,Yuchen. Zhang, Baoxiang Zhang. Luo Xiaodong. Elevated-temperature Plasticity and mechanical properties of a rare earth-modified Mg-Zn-Al alloy.materials Letters.65(2011)944-947. https://doi.org/10.1016/j.matlet.2011.01.001.

[4] Singh, Alok. Tsai, A.P. On the cubic W phase and its relationship to the icosahedral phase in Mg-Zn-Y alloys.Scr. Mater.49(2003)143-148. https://doi.org/10.1016/S1359-6462(03)00217-3.

[5] B. Baburao, N.H. Kumar, A. Edukondalu, et al., Influence of Er/Fe substitution on Mg-Zn nanoparticles' electromagnetic properties and applications, Braz. J. Phys. 53 (2023) 91, https://doi.org/10.1007/s13538-023-01300-1.

[6] Cheng,Du. Hoglund,Eric R. Wang, Kang. Howe, James M. Agnew, Sean R. Zhou, Bi-Cheng. Atomic structures of ordered monolayer GP zones in Mg-Zn-x (X=ca,Nd) systems. Scr. Mater.. 216(2022)114744. https://doi.org/10.1016/j.scriptamat.2022.114744.

[7] Wang,Qing-feng. LI, Han. LI, Shu-bo. WANG, Zhao-hui. DU, Wen-bo. Microstructure evolution and mechanical properties of extruded Mg-12Zn-1.5Er alloy. Trans.Nonferrous Met.Soc.21(2011)874-879. https://doi.org/10.1016/S1003-6326(11)60796-6.

[8] Wasiur-Rahman, S. Medraj, M. Critical assessment and thermodynamic modeling of the binary Mg-Zn,Ca-Zn and ternary Mg-Ca-Zn Systems.Intermetallics.17(2009) 847-864. https://doi.org/10.1016/j.intermet.2009.03.014.

[9] Zhang, Jing. Yuan, Fuqing. Du, Yong. Enhanced age-Strengthening by two-step progressive solution treatment in an Mg-Zn-Al-Re alloy. Materials & Design (1980-2015).52(2013)332-336. https://doi.org/10.1016/j.matdes.2013.05.074.

[10] Miao,Hongwei. Huang,Hua. Fan, Shihao. Tan, Jinyun. Wang, Zhongchang. Ding, Wenjiang. Yuan, Guangyin. Nanoscale precipitation in deformed dilute alloying Mg-Zn-Gd alloy.Materials & Design.196(2020)109122. https://doi.org/10.1016/j.matdes.2020.109122.

[11] Yamasaki,Michiaki. Hashimoto,Kenji. Hagihara, Koji. Kawamura, Yoshihito. Effect of multimodal microstructure evolution on mechanical properties of Mg-Zn-Y extruded alloy.Acta Mater.59(2011)3646-3658. https://doi.org/10.1016/j.actamat.2011.02.038.

[12] Wang,Dan. Ma, Xiaochun. Wu, Ruizhi. Wu, Huajie. Wang, Jiahao. Zhang, Shun. Zhang,jinghuai. Hou, Legan. Effect of extrusion plus rolling on damping capacity and mechanical properties of Mg-Y-Er-Zn-Zr alloy. Mater.Sci.Eng.A.830(2022) 142298. https://doi.org/10.1016/j.msea.2021.142298.

[13] X.Q. Liu, D.S. Zhao, L. Ye, Y.L. Zhuang, S.B. Gao, J.B. Wang, Effect of Er contents on the microstructure of long period stacking ordered phase and the corresponding mechanical properties in Mg-Dy-Er-Zn alloys, Mater. Sci. Eng. A 718 (2018) 461–467, https://doi.org/10.1016/j.msea.2018.01.066.

[14] Ghosh,P. Mezbahul-Islam, M. Medraj,M. Critical assessment and thermodynamic modeling of Mg-Zn, Mg-Sn,Sn-Zn and Mg-Sn-Zn systems.calphad.36(2012)28-43. https://doi.org/10.1016/j.calphad.2011.10.007.

[15] Xue,Hansong. Liu, Song. Xie, Wei. Zhou, Yang. peng, Jianbo. Pan, Haitao. Zhang, Dingfei. pan, Fusheng. Improvement of mechanical properties of hot extruded and aged Mg-Zn-Mn-Sn alloy through Dy addition. Mater. Charact.187(2022)111874. https://doi.org/10.1016/j.matchar.2022.111874.

[16] Singh, Alok. Osawa,Yoshiaki. Somekawa, H. Mukai,T. Ultra-fine grain size and isotropic very high strength by direct extrusion of chill-cast Mg-Zn-Y alloys containing quasicrystal phase. Scr.Mater.64(2011)661-664. https://doi.org/10.1016/j.scriptamat.2010.12.016.

[17] N. Hari kumar, D. Ravinder, A. Edukondalu, Effect of Ce3+ ion doped Ni-Zn ferrites: Structural, optical and low temperature magnetic properties, Chin. J. Phys. 81 (2023) 171–180, https://doi.org/10.1016/j.cjph.2022.11.019.

[18] Wang,Jian. Zhang,Yi-Nan. Hudon,Pierre. Jung,In-Ho. Chartrand,Patrice. Medraj, Mamoun. Experimental study of the crystal structure of the Mg15-xZnxSr3 ternary solid solution in the Mg-Zn-Sr System at 300°C.Materials & Design.86(2015)305-312. https://doi.org/10.1016/j.matdes.2015.07.038.

[19] ZHAO,Xian-feng. LI,Shu-bo. WANG, Qing-feng. DU,Wen-bo. LIU,Ke. Effects of heat treatment on microstructure and mechanical properties of Mg-5Zn-0.63Er alloy. Trans. Nonferrous Met.Soc.23(2013)59-65. https://doi.org/10.1016/S1003-6326(13)62429-2.

[20] Li, Jianhui. Du, Wenbo. Li,Shubo. Wang,Zhaohui. Tensile and creep behaviors of Mg-5Zn-2.5Er alloy improved by icosahedral quasicrystal.Mater.Sci.Eng.A.527 (2010)1255-1259. https://doi.org/10.1016/j.msea.2009.10.006.

[21] WANG, Shao-hua. MENG,Ling-gang. YANG,Shou-jie. FANG,Can-feng. HAO,Hai. DAI, Sheng-long. ZHANG,Xing-guo. Microstructure of Al-Zn-Mg-Cu-Zr-0.5Er alloy under as-cast and homogenization conditions.Trans.Nonferrous Met.Soc.21(2011) 1449-1454. https://doi.org/10.1016/S1003-6326(11)60880-7.

[22] Zhang,Xiaolong. Wang,Zhaohui. Du,Wenbo. Liu,Ke. Li,Shubo. Microstructures and mechanical properties of Mg-13Gd-5Er-1Zn-0.3Zr alloy.Materials & Design.58 (2014)277-283. https://doi.org/10.1016/j.matdes.2014.01.058.

[23] Ji, chengwei. Ma,Aibin. Jiang,Jinghua. Mechanical properties and corrosion behavior of novel Al-Mg-Zn-Cu-Si lightweight high entropy alloys.J.Alloys Compd.900(2022)163508. https://doi.org/10.1016/j.jallcom.2021.163508.

[24] Yang,Youwen. Ling, Chenrong. Li,Yageng. Peng,Shuping. Xie, Deqiao. Shen,Lida. Tian, Zongjun. Shuai,Cijun.Microstructure development and biodegradation

behavior of additively manufactured Mg-Zn-Gd alloy with LPSO structure.J.Mater. Res.Technol.144(2023)1-14. https://doi.org/10.1016/j.jmst.2022.09.059.
[25] FAN,Wen-xue. BAI,Yu. LI, Guang-yang. CHANG,Xing-yang. HAO,Hai. Enhanced mechanical properties and formability of hot-rolled Mg-Zn-Mn alloy by Ca and Sm alloying.Trans.Nonferrous Met.Soc.32(2022)1119-1132. https://doi.org/10.1016/S1003-6326(22)65860-6.
[26] Itoi,T. Inazawa,T. Yamasaki,M. Kawamura,Y. Hirohashi, M. Microstructure and mechanical properties of Mg Zn Y alloy sheet prepared by hot-rolling.Mater.Sci. Eng.A.560(2013)216-223. https://doi.org/10.1016/j.msea.2012.09.059.
[27] Jihua,Chen. Zhenhua,Chen. Hongge,Yan. Fuquan, Zhang. Kun,Liao. Effects of Sn addition on microstructure and mechanical properties of Mg-Zn-Al alloys. J.Alloys Compd.461(2008)209-215. https://doi.org/10.1016/j.jallcom.2007.07.066.
[28] Shahzad,M. Wagner,L. The role of Zr-rich cores in strength differential effect in an extruded Mg-Zn-Zr alloy.J.Alloys Compd.486(2009)103-108. https://doi.org/10.1016/j.jallcom.2009.06.123.
[29] Zhang,Li. Zhang,Jinghuai. Leng,Zhe. Liu,Shujuan. Yang,Qiang. Wu,Ruizhi. Zhang, Milin.Microstructure and mechanical properties of high-performance Mg-Y-Er-Zn extruded alloy.Materials & Design (1980-2015).54(2014)256-263. https://doi.org/10.1016/j.matdes.2013.08.048.
[30] Liang,P. Seifert,H.J. Lukas,H.L. Ghosh,G. Effenberg,G. Aldinger,F.Thermodynamic modeling of the Cu-Mg-Zn ternary system. calphad.22(1998)527-544. https://doi.org/10.10160364-5916(99)00009-7.
[31] LI,Han. DU,Wen-bo. LI,Jian-hui. LI,Shu-bo. WANG, Zhao-hui. Creep properties and controlled creep mechanism of as-cast Mg-5Zn-2.5Er alloy.Trans.Nonferrous Met. Soc.20(2010)1212-1216. http://doi.org/10.1016/S1003-6326(09)60280-6.
[32] Abdullah,M.H. Yusoff,A.N. Complex impedance and dielectric properties of an Mg Zn ferrite.J.Alloys Compd.233(1996)129-135.http://doi.org/10.s1016/0925-8388(96)80044-2.
[33] V. Ludhiya, N. Hari kumar, D. Ravinder, Avula Edukondalu, Structural, optical, dielectric and magnetic properties of Nd3+ ion substituted Ni-Mg-Cu spinel ferrites, Inorg. Chem. Commun. 150 (2023), 110558, https://doi.org/10.1016/j.inoche.2023.110558.
[34] N. Hari kumar, D. Ravinder, A. Edukondalu, Synthesis, structural, antimicrobial activity and dielectric properties of Ce3+-doped Ni–Zn nano-ferrites, Appl. Phys. A 128 (2022) 978, https://doi.org/10.1007/s00339-022-06096-6.
[35] Juying,Wei. Jihua,Chen. Hongge,Yan. Bin,Su. Guanghao,Zhang. Xi,He. Microstructure, Tensile Properties and Creep Resistance of Sub-rapidly Solidified Mg-Zn-Sn-Al-Ca Alloys.RARE METAL MAT ENG.43(2014)2602-2608. https://doi.org/10.1016/S1875-5372(15)60010-8.
[36] Longgang,Hou. Jiajia, Yu, Di,Zhang. Linzhong,Zhuang. Li,Zhou. Jishan,Zhang. Corrosion Behavior of Friction Stir Welded Al-Mg-(Zn) Alloys.RARE METAL MAT ENG.46(2017)2437-2444. https://doi.org/10.1016/S1875-5372(17)30212-6.
[37] Jihua, Chen. Juying,Wei. Hongge,Yan. Bin,Su. Xueqiang,Pan.Effects of cooling rate and pressure on microstructure and mechanical properties of sub-rapidly solidified Mg-Zn-Sn-Al-Ca alloy.Materials & Design 45(2013) 300-307. https://doi.org/10.1016/j.matdes.2012.09.003.
[38] DU,Yu-zhou. LIU,Dong-jie. GE, Yan-feng. JIANG,Bai-ling.Effects of deformation parameters on microstructure and texture of Mg-Zn-Ce alloy.Trans.Nonferrous Met.Soc.30(2020)2658-2668. https://doi.org/10.1016/S1003-6326(20)65410-3.
[39] WANG,Qing-feng. DU,Wen-bo. LIU,Ke. WANG,Zhao-hui. LI,Shu-bo. Effect of Zn addition on microstructure and mechanical properties of as-cast Mg-2Er alloy. Trans.Nonferrous Met.Soc.24(2014)3792-3796. https://doi.org/10.1016/S1003-6326(14)63534-2.
[40] A.V. Mikhaylovskaya, O.A. Yakovtseva, V.V. Cheverikin, A.D. Kotov, V.K. Portnoy, Superplastic behavior of Al-Mg-Zn-Zr-Sc-based alloys at high strain rates, Mater. Sci. Eng. A 659 (2016) 225–233, https://doi.org/10.1016/j.msea.2016.02.061.
[41] HE,Sheng-ying. SUN,Yue. CHEN Min-fang. LIU De-bao. YE,Xin-yu. Microstructure and properties of biodegradable β-TCP reinforced Mg-Zn-Zr composites.Trans. Nonferrous Met.Soc.21(2011)814-819. https://doi.org/10.1016/S1003-6326(11)60786-3.
[42] Banoth Baburao, N. Hari kumar, Avula Edukondalu, M. Venkata Narayana, D. Ravinder, optical, DC electrical, thermo-electric, dielectric and magnetic properties of $Mg_{0.8}Zn_{0.2}Gd_xFe_{2-x}O_4$ nanoparticles synthesised by citrate-gel auto combustion method. Inorg. Chem. Commun. 148, 110355 (2023). **https://doi.org/10.1016/j.inoche.2022.110355.**
[43] Singh,Alok. Somekawa,H. Mukai, T. High temperature processing of Mg-Zn-Y alloys containing quasicrystal phase for high strength.Mater.Sci.Eng.A.528(2011)6647-6651. https://doi.org/10.1016/j.msea.2011.05.001.
[44] Wang,Guangang. Huang,Guangsheng. Chen,Xiang. Deng,Qianyuan. Tang,Aitao. Jiang, Bin. Pan ,Fusheng.Effects of Zn addition on the mechanical properties and texture of extruded Mg-Zn-Ca-Ce magnesium alloy sheets.Mater.Sci.Eng.A.705(2017)46-54. https://doi.org/10.1016/j.msea.2017.08.036.
[45] R. Sterzel, E. Dahlmann, A. Langsdorf, W. Assmus, Preparation of Zn-Mg-rare earth quasicrystals and related crystalline phases, Mater. Sci. Eng. A 294–296 (2000) 124–126, https://doi.org/10.1016/S0921-5093(00)01313-7.